

Stratospheric Age-of-Air: Sensitivity to Finite Volume Remapping Algorithm

Clara Orbe^{1,2}, Lawrence L. Takacs^{3,4}, Amal El Akkraoui^{3,4},
Krzysztof Wargan^{3,4}, Andrea Molod³

¹NASA Goddard Institute for Space Studies, New York, NY

²Department of Applied Physics and Applied Mathematics, Columbia University, New York, NY

³Global Modeling and Assimilation Office, NASA Goddard Space Flight Center, Greenbelt, MD

⁴Science Systems and Applications, Inc., Lanham, MD, USA

Key Points:

- The stratospheric mean age-of-air simulated in GEOS is sensitive to the remapping scheme used within the finite-volume dynamical core.
- This sensitivity in the age-of-air approaches 30% and imprints on the simulated distributions of several long-lived chemical trace gases, including nitrous oxide and methane.
- The age-of-air sensitivities primarily reflect changes in resolved wave convergence over the Northern Hemisphere midlatitude stratosphere, which impact mean upwelling within the tropical lower stratosphere.

Corresponding author: Clara Orbe, clara.orbe@nasa.gov

18 **Abstract**

19 Accurately modeling the large-scale transport of trace gases and aerosols is critical for interpreting past (and projecting future) changes in atmospheric composition. 20 Simulations of the stratospheric mean age-of-air continue to show persistent biases among 21 chemistry climate models, although the drivers of these biases are not well understood. 22 Here we identify one driver of simulated stratospheric transport differences among various 23 NASA Global Earth Observing System (GEOS) candidate model versions under consideration 24 for the upcoming GEOS Retrospective analysis for the 21st Century (GEOS-R21C). In particular, 25 we show that the simulated age-of-air values are sensitive to the so-called “remapping” 26 algorithm used within the finite-volume dynamical core, which controls how individual 27 material surfaces are vertically interpolated back to standard pressure levels after each 28 horizontal advection time step. Differences in the age-of-air resulting from changes 29 within the remapping algorithm approach ~ 1 year over the high latitude middle 30 stratosphere - or about 30% climatological mean values - and imprint on several trace 31 gases, including methane (CH_4) and nitrous oxide (N_2O). These transport sensitivities 32 reflect, to first order, changes in the strength of tropical upwelling which are driven by 33 changes in resolved wave convergence over northern midlatitudes as (critical lines of) 34 wave propagation shift in latitude. Finally, we show that degradations in the simulation 35 of the age-of-air, stratospheric upwelling and zonal wind climate statistics derived from 36 30-year-long atmosphere-only (AMIP) experiments, translate to degraded skill in the 37 analysis states used within data assimilation experiments. Our results strongly support 38 continued examination of the role of numerics in contributing to transport biases in 39 composition modeling. 40

41 **Plain Language Summary**

42 Large-scale transport plays a crucial role in distributing climatically important trace 43 constituents in the atmosphere, especially in the stratosphere where transport largely 44 determines the chemical lifetimes of trace gases. One summary of transport in the stratosphere 45 is the “mean age” or the mean transit time since air at a point in the stratosphere was 46 last in the troposphere. Current models used for simulating stratospheric composition 47 produce a range of simulated ages, although these differences are poorly understood. 48 Among other factors, model numerics play a critical role in transport, but few studies 49 have explored the sensitivity of the mean age to the choice of numerical scheme employed 50 within different dynamical cores. Here we use one model to show that the mean age is 51 sensitive to the so-called “remapping” algorithm used within the finite-volume dynamical 52 core that controls how individual material surfaces are vertically interpolated back to 53 standard pressure levels after each horizontal advection time step. This reflects 54 sensitivities in the representation of how waves propagate from the troposphere into the 55 stratosphere. This work suggests that model numerics can be an important factor in 56 contributing to differences in simulated transport among models.

57 **1 Introduction**

58 The chemical and radiative properties of the troposphere and lower stratosphere are 59 strongly influenced by the stratosphere-troposphere exchange of mass and tracers (e.g., 60 Morgenstern and Carver (2001); Hegglin et al. (2006); Pan et al. (2007)). Properly 61 simulating the stratospheric circulation and its influence on atmospheric composition in 62 earth system models is important for capturing past decadal trends in surface climate, 63 particularly in response to changes in Southern Hemisphere ozone depletion (e.g., Son et 64 al. (2009); Polvani et al. (2011)). In the Northern Hemisphere (NH), the stratospheric 65 circulation’s coupling to ozone could represent an important feedback on the climate’s 66 response to future increases in greenhouse gases (GHGs), especially over the North 67 Atlantic (e.g., Chiodo and Polvani (2019)). On shorter subseasonal timescales, stratospheric

68 ozone changes associated with strong polar vortex states may also modulate Arctic sea
69 level pressure and surface temperatures (e.g., Ivy et al. (2017); Oehrlein et al. (2020)),
70 so much so that seasonal forecast systems employing prognostic ozone show suggestions
71 of increased signal-to-noise ratio in predictions of the North Atlantic Oscillation (B. M. Monge-
72 Sanz et al. (2022)).

73 Key to accurately simulating a consistent representation of coupling between strato-
74 spheric dynamics and chemical trace gases is ensuring that a model’s underlying trans-
75 port circulation is properly represented. To this end, much effort has been paid to de-
76 veloping and refining so-called “tracer-independent” metrics of transport (Holzer and Hall
77 (2000)) such as the mean age-of-air (Hall and Plumb (1994)) and to applying these mea-
78 sures to rigorously evaluate model transport characteristics in chemistry climate mod-
79 els (CCMs) (e.g., Hall et al. (1999); Orbe et al. (2018); Dietmüller et al. (2018); Aba-
80 los et al. (2020)).

81 While the assessment of CCMs participating in the SPARC Chemistry Climate Model
82 Validation (SPARC CCMVal) effort showed a marked improvement in simulated trans-
83 port characteristics relative to previous intercomparisons (J. Neu et al. (2010)), more re-
84 cent analysis of models participating in the SPARC Chemistry Climate Modeling Ini-
85 tiative (CCMI) (Eyring et al. (2013)) do not demonstrate any improvement (Dietmüller
86 et al. (2018), see their Figure 3). In particular, although some models produce mean age
87 values that agree well with observational estimates, the CCMI intermodel spread is \sim
88 50%, with models generally simulating transport that is too vigorous, relative to obser-
89 vations. While documenting these transport differences among models is straightforward,
90 understanding the drivers of this spread remains a key challenge and there is still no con-
91 sensus on what is causing the large spread in simulated ages among the current gener-
92 ation of CCMs.

93 A key challenge in identifying the drivers of age-of-air – and other stratospheric trans-
94 port – biases is that they reflect the time-integrated effects of advection by the residual
95 mean circulation and eddy diffusive mixing, or the quasi-random transport due to the
96 breaking of Rossby waves (e.g., Holton et al. (1995); Plumb (2002)). Given that the in-
97 fluences of mixing and advection are not easily separable, studies have come to differ-
98 ent conclusions about sources of age biases in models. In particular, the analysis of the
99 CCMVal models showed a strong correlation between the intermodel spread in the age-
100 of-air and lower stratospheric tropical upwelling, whereas Dietmüller et al. (2018) showed
101 that the age spread among the CCMI models was driven by differences in mixing. While
102 future attempts to further distinguish between sources of age biases using either simpli-
103 fied “leaky pipe” models (Plumb (1996); J. L. Neu and Plumb (1999)) or more complete
104 measures of the transport circulation such as the “age spectrum” (e.g., Hall and Plumb
105 (1994); Waugh and Hall (2002))) may prove enlightening, at present there is no consen-
106 sus on what is causing large simulated age-of-air biases in models.

107 One potential limitation of previous work based on multi-model intercomparisons
108 is that many aspects of model formulation can influence both stratospheric upwelling and
109 mixing. Thus, while intercomparisons are useful for identifying common model biases,
110 understanding the drivers of these biases is difficult absent single model-based process
111 studies. Among these, several aspects of model formulation have been identified as in-
112 fluencing simulated mean age distributions. As the mean age is sensitive to vertical mo-
113 tion in the lowermost stratosphere, these include large sensitivities to vertical resolution
114 (Orbe et al. (2020)) and to spurious vertical mixing either introduced in vertical coor-
115 dinate transformations in offline chemical transport models (B. Monge-Sanz et al. (2007))
116 or through use of assimilated winds performed either in offline (e.g., Legras et al. (2004))
117 or online data assimilation and “nudged” configurations (e.g., Pawson et al. (2007); Orbe
118 et al. (2017); Davis et al. (2022)). These age sensitivities can be still further amplified,
119 depending on whether or not parameterized gravity waves are included (Eichinger et al.
120 (2020)).

121 By comparison, sensitivities of the mean age to underlying tracer numerics have
 122 been less well examined, although Eluszkiewicz et al. (2000) documented a large sensi-
 123 tivity in simulated age-of-air values to the choice of advection scheme. More recently,
 124 Gupta et al. (2020) showed differences of $\sim 25\%$ in the age-of-air across identical exper-
 125 iments performed using four different dynamical cores, especially between those using
 126 spectral versus finite-volume schemes. The experiments employed in that study, how-
 127 ever, were highly idealized and it is not clear if the strong influence of tracer numerics
 128 that they identified is also realized in more comprehensive model simulations with moist
 129 physics, especially in the context of model development as carried out in operational mod-
 130 eling centers.

131 **Amal, can you please improve my introduction of R21C in the next paragraph, fo-**
 132 **ocusing on distinguishing between the met reanalysis versus R21C-Chem replay (with a**
 133 **brief description of replay)? The concept of DAS also needs to be briefly introduced.**

134 To better elucidate this influence of tracer numerics on the transport properties sim-
 135 ulated in a comprehensive global model context, here we document the sensitivity of the
 136 stratospheric mean age in several recent versions of the NASA Global Earth Observing
 137 System (GEOS) general circulation model (Molod et al., 2015) that represent different
 138 stages in model development since the Modern-Era Retrospective Analysis for Research
 139 and Applications Version 2 (MERRA-2; Gelaro et al. (2017)). Our focus on transport
 140 evaluation is in wake of the upcoming release of the GEOS Retrospective analysis for
 141 the 21st Century (GEOS-R21C), which will serve as an intermediate reanalysis between
 142 MERRA-2 and MERRA-3 (~ 2025 **Amal, please correct this date**). As GEOS-R21C will
 143 be used to drive an off-line chemistry reanalysis (GEOS-R21C-Chem) it is imperative
 144 that it produces a credible representation of transport processes.

145 In particular, here we document how in the process of evaluating candidate sys-
 146 tems for GEOS-R21C we found that the mean age was ~ 1 younger than the values sim-
 147 ulated in the model version used to produce MERRA-2 (Figure 1). The model versions
 148 shown in Figure 1 reflect more than 10 years’ worth of accumulated changes in model
 149 development, most notably changes in radiation, parameterized convection and, as we
 150 focus on here, changes in the algorithm used to transform advected fields from Lagrangian
 151 levels to fixed pressure levels after each horizontal advection time step. We show that
 152 slight modifications in this so-called “remapping” algorithm are the primary driver of
 153 the age-of-air changes exhibited in recent GEOS-R21C candidate model versions, a re-
 154 sult which may have broader implications for other general circulation models using fi-
 155 nite volume (FV) dynamical cores. We begin by discussing methods in Section 2 and present
 156 key results and conclusions in Sections 3 and 4, respectively.

157 2 Methods

158 2.1 Model Configurations

159 Here we present results from several versions of GEOS spanning MERRA-2 to more
 160 recent candidates for GEOS-R21C. Among these model versions, a subset are more “of-
 161 ficial” as they have been documented and/or employed in recent model intercomparisons
 162 and are highlighted in Figure 1. In particular, these include an intermediary model ver-
 163 sion that was used in Phase 1 of CCMI and documented in Orbe et al. (2017) (Fig. 1,
 164 red line). A more recent model version that was used in the CCMI Phase 2 simulations
 165 (correspondence with Michael Manyin) is also shown (Fig. 1, green line). These two con-
 166 figurations correspond to the Heracles 5.3 and Icarus 3.2 versions of the GEOS system,
 167 respectively (**Amal: I need the corresponding DAS tag names, if they exist**).

168 We begin by comparing 10-year (2000-2010) climatological mean zonally averaged
 169 age-of-air profiles at 50 hPa across this subset of model versions, derived from 30-year
 170 long atmosphere-only (AMIP) integrations constrained with observed sea surface tem-

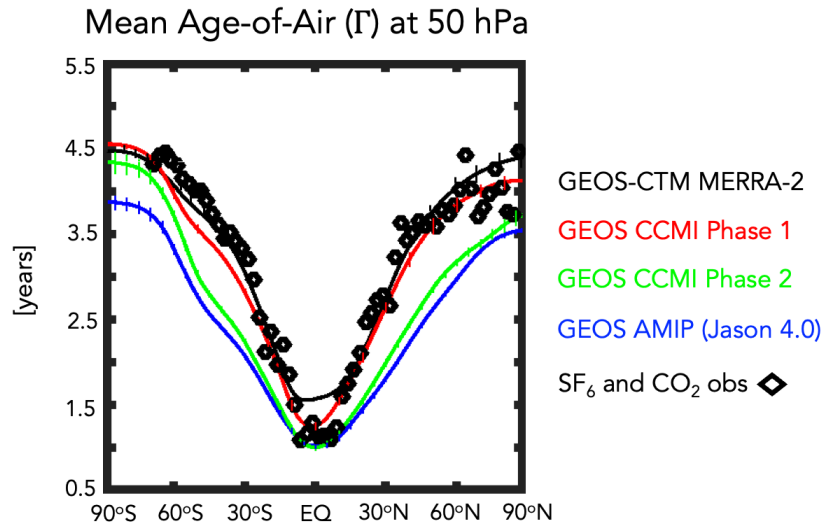


Figure 1. The 2000-2010 climatological annual mean meridional profile of the stratospheric mean age-of-air (Γ), evaluated at 50 hPa. Results from a GEOS-CTM integration constrained with MERRA-2 meteorological fields (black line) as well as free-running GEOS simulations using a model configuration for CCM1 Phase 1 (red line), CCM1 Phase 2 (green line) and a more recent GEOS-FP development tag (Jason 4.0, blue line) are shown. The GEOS model versions to which these configurations correspond are the Heracles 5.3, Icarus 3.2, and Jason 4.0 tags, respectively. All simulations are constrained with the same (observed) historical sea surface temperatures. Diamonds correspond to SF₆ and CO₂ in situ based estimates of Γ from Boering et al. (1996) and Engel et al. (2009). Vertical dashed lines denote $\pm\sigma$, the standard deviation of Γ over 2000-2010, for each model simulation.

171 peratures (Figure 1). First, we note that the profiles for the CCMI Phase 1 version of
 172 the model are very close to observations (black stars), consistent with the
 173 “GEOSCCM” documented age characteristics reported in Dietmüller et al. (2018) (see
 174 their Figure 3). In addition, while passive tracers were not integrated within MERRA-
 175 2, results using the GEOS chemistry transport model (GEOS-CTM, Kouatchou et al.
 176 (2015)) constrained with MERRA-2 meteorological fields (black line) also exhibits good
 177 agreement with observed values. This good agreement between the CTM-generated age-
 178 of-air and the observations is consistent with results from a previous GEOS-CTM sim-
 179 ulation (constrained with MERRA) that was documented in Orbe et al. (2017).

180 Moving to more recent development versions of the model (green and blue lines),
 181 however, reveals a reduction in the mean age by ~ 1 year over both southern and north-
 182 ern high extratropical latitudes, or a decrease of $\sim 20\text{-}30\%$ relative to MERRA-2. As dis-
 183 cussed earlier, the green line refers to the CCMI Phase 2 model version, whereas the blue
 184 line refers to an undocumented candidate version (model tag Jason 4.0) that corresponds
 185 best to a model configuration similar to what is used in the GEOS forward processing
 186 (FP) numerical weather prediction system (**Amal: What is FP DAS version correspond-**
 187 **ing to Jason 4.0 (or similar model)?**). Note that this decrease in the climatological age
 188 in both model versions far exceeds the (internal) variations in mean age that occur in-
 189 terannually (vertical bars on solid lines).

190 There are numerous development updates in the model that have occurred since
 191 MERRA-2. Therefore, after discussing the model configurations highlighted in Figure
 192 1 in Section 3.1, we then present results from targeted experiments aimed at successively
 193 undoing these model updates (Section 3.2). Among those aspects most likely impact-
 194 ing the stratospheric transport circulation, these include updates to the radiation scheme,
 195 moving from Chou and Suarez (1994) in the shortwave and Chou (1990, 1992) in the long-
 196 wave to the Rapid Radiative Transfer Model for GCMS (RRTMG; Iacono et al. (2008)).

197 In addition to the radiation changes, another more consequential model develop-
 198 ment was made to the handling of the remapping algorithm within the model’s FV dy-
 199 namical core (Lin, 2004). In particular, vertical motion is realized through the Lagrangian
 200 transport of the “floating” vertical coordinate such that after each horizontal advection
 201 step the individual material surfaces are vertically interpolated back to standard pres-
 202 sure levels through FV’s so-called “REMAP” algorithm. This is needed because the La-
 203 grangian surfaces that vertically bound the finite volumes will eventually deform, neg-
 204 atively impacting the accuracy of the horizontal-to-Lagrangian-surface transport and the
 205 computation of the pressure-gradient terms.

206 There are various user-defined parameters and decisions that are made within the
 207 remapping algorithm. In its current implementation this involves 1) fitting piecewise parabolic
 208 (hereafter PPM) functions to input layer-mean values of T, U, V, Q and tracers; 2) cal-
 209 culating PPM functions to output layer edges; and 3) integrating PPM functions between
 210 output layer edges to produce new layer-mean values of T, U, V, Q and tracers. Note
 211 that T, U, V, Q, C_p , K and Φ correspond to temperature, zonal wind, meridional wind,
 212 specific humidity, specific heat capacity and kinetic and potential energy, respectively.
 213 This implementation setup is consistent with what is currently being used in most re-
 214 cent GEOS model versions (i.e. blue and green lines, Figure 1) and hereafter is referred
 215 to as REMAP Option 2 (Table 1, left).

216 The alternative version – which best mimics what was used in MERRA-2 – involves
 217 two main changes to this procedure and is hereafter referred to as REMAP Option 1 (Ta-
 218 ble 1, right; red line in Figure 1). First steps 1) and 3) are performed only for U, V, Q
 219 and tracers (not T). Second, three additional steps after 3) are added, the first two of
 220 which involve calculating total energy (TE) at input mid-layer pressures and then per-
 221 forming cubic interpolation and a posteriori integral conservation at output mid-layer

Table 1. Finite Volume Remapping Algorithm: The two versions examined in this study control how individual material surfaces are vertically interpolated back to standard pressure levels. REMAP Options 2 and 1 corresponds to the configurations used in more recent (green and blue lines, Figure 1) and older (red and black lines, Figure 1) model configurations, respectively. Here T, U, V, Q, C_p , K and Φ correspond to temperature, zonal wind, meridional wind, specific humidity, specific heat of air at constant pressure and kinetic and potential energy, respectively.

Step	REMAP Option 2 (CTRL)	REMAP Option 1 (MERRA-2)
1	Fit PPM functions to input layer-mean T, U, V, Q and tracers	Fit PPM functions to input layer-mean U, V, Q and tracers
2	Calculate PPM to output layer edges	Calculate PPM to output layer edges
3	Integrate PPM functions between output layer edges to produce new layer-mean T, U, V, Q and tracers	Integrate PPM functions between output layer edges to produce new layer-mean U, V, Q and tracers
4	n/a	Calculate TE = $C_p T + K + \Phi$ at input mid-layer pressures
5	n/a	Calculate TE at output mid-layer pressures using cubic interpolation and a-posteriori integral conservation
6	n/a	Construct “remapped” T via $T = (TE - K - \Phi)/C_p$

222 pressures. Finally, temperatures are “remapped” from total energy via $T = (TE - K -$
 223 $\Phi)/C_p$.

224 When examining Table 1, it is important to note that Options 1 and 2 differ in two
 225 main respects. Of these, we find that the simulated ages are most sensitive to the inter-
 226 polation that occurs within step 5 in REMAP Option 1 (Table 1). The use of TE (as
 227 opposed to T), by comparison, is less consequential (Appendix A, Figure A1 (a)). To
 228 this end, the sensitivity experiments discussed in the next section mainly focus on iden-
 229 tifying the age sensitivities in response to changes in the interpolation scheme used in REMAP
 230 Option 1, not to differences between the use of TE versus T.

231 Finally, it is worth noting other important model development changes that occurred
 232 related to the parameterization of deep convection (Grell and Freitas (2014); Freitas et
 233 al. (2018)) which could, potentially, have an indirect impact on the stratospheric circu-
 234 lation through their influence on wave generation in the troposphere. As we show, how-
 235 ever, while these have a substantial impacts upon their incorporation in a nonhydrostatic
 236 version of the model on characteristics like the diurnal cycle of precipitation (Arnold et
 237 al. (2020)) and on convective transport within the troposphere (Freitas et al. (2020)),
 238 their indirect influence on the stratosphere is less impactful.

239 2.2 Model Experiments

240 2.2.1 AMIP vs. EMIP vs. DAS

241 We begin our analysis by interpreting the results shown in Figure 1, which are all
 242 based on historical AMIPs that were performed at the same cubed sphere C180 (approx-
 243 imately half-degree) horizontal resolution. As they represent more “official” model ver-
 244 sions they serve as an important motivation for the experiments that follow. However,

245 a clean/meaningful analysis of this set of runs is nonetheless hampered by the structural
246 model differences between them.

247 In order to investigate the drivers of the differences in Figure 1 we perform targeted
248 model experiments aimed at further disentangling the influence of recent model devel-
249 opment changes on stratospheric transport properties (Table 2). In order to evaluate im-
250 pacts on transport climate statistics, we consider both a set of climatological AMIP (rows
251 1-4) as well as so-called “EMIP” (rows 5-7) experiments. Impacts on the data assimi-
252 lation analysis state are then evaluated using one-year-long DAS experiments (rows 8-
253 9).

254 Among the first two experiment types, the AMIP simulations are carried out at
255 C180 resolution and are used to infer the climate characteristics of the different model
256 configurations. The “EMIP” experiments – ensembles of 3-month-long integrations ini-
257 tialized on approximately November 15 of each year between 1985 and 2015 – are also
258 used to infer impacts on simulated transport climate. As they are more computation-
259 ally efficient than AMIPs, however, they are performed at both C180 and C360 resolu-
260 tions in order to examine the sensitivity of our results to changes in horizontal resolu-
261 tion.

262 As shown in Appendix B, comparisons of the December-January-February (DJF)
263 vertical profile of tropical upwelling show excellent agreement between EMIP and AMIP
264 integrations carried out using the same model configuration (Appendix Figure B1). This
265 somewhat incidental result, represents, to the best of our knowledge, the first time that
266 EMIP-based statistics have been shown to converge well to those from AMIPs for the
267 stratospheric metrics considered in this study. This suggests that EMIPs may provide
268 a computationally more efficient alternative to AMIPs for use in quickly ascertaining the
269 impacts of model changes.

270 *2.2.2 Model Development Changes*

271 In terms of the precise development changes examined, we begin by defining a con-
272 trol experiment (CTRL; Table 2, row 1), which best corresponds to the blue line shown
273 in Figure 1. Then we define three new AMIP experiments based off this control that are
274 used to distinguish between the age changes resulting from changes in radiation versus
275 changes in the handling of the REMAP algorithm (Section 3.2.1).

276 Specifically, these include experiments in which we revert back from RRTMG to
277 Chou and Suarez (1994) in the shortwave (CSRAD; Table 2, row 2), b) revert back to
278 the MERRA-2 REMAP approach (i.e. REMAP Option 1) (M2REMAP; Table 2, row
279 3) and c) combine these two changes (CSRAD+M2REMAP; Table 2, row 4). Note that
280 we have also have performed experiments in which RRTMG is reverted back to Chou
281 (1990) in the longwave, but these changes are less impactful, compared to the shortwave
282 radiation changes (not shown).

283 As shown in Section 3.2.1, the M2REMAP experiment produces the largest changes
284 in age-of-air, compared to the altered radiation experiments. To this end, we focus the
285 remainder of our investigation (Section 3.2.2) on examining a clean set of EMIP exper-
286 iments run at both C180 and C360 horizontal resolutions that distinguish the impact of
287 REMAP Option 1 versus Option 2 on simulated transport. In particular, we perform
288 three sensitivity experiments that differ from each other only in terms of the calculation
289 of TE at the mid-layer pressure levels, which we perform using a linear (LINEAR; Ta-
290 ble 2, row 5), quadratic (QUADRATIC; Table 2, row 6) and cubic interpolation (CU-
291 BIC; Table 2, row 7) scheme, with the latter corresponding to the approach that was used
292 in MERRA-2. Note that, while the LINEAR and QUADRATIC experiments do not ac-
293 tually correspond to any of the development tags shown in Figure 1, they highlight the
294 large sensitivity of the mean age to changes in the interpolation scheme that may oth-

Table 2. GEOS Model Experiments: Targeted GEOS model experiments based off a control experiment (row 1) were carried out to identify the influence of radiation (row 2) and the FV remapping algorithm changes since MERRA-2 (row 3), as well as their combined influence (row 4). Sensitivities within the FV remapping algorithm were further explored with respect to the order of the interpolation scheme used to calculate TE at output mid-layer pressure levels (rows 5-7). Experiments in rows 1-4 are 30-year-long AMIPs run at C180 resolution, whereas rows 5-7 refer to 30-member 3-month-long (DJF) EMIP experiments. Both AMIPs and EMIPs are used for climate statistic evaluation (see Appendix A for more on the correspondence between the two). By comparison, rows 8-9 refer to 1-year-long DAS runs used for evaluation of the analysis state. Both DAS and EMIP experiments are run at C180 and C360 horizontal resolutions.

Experiment Name	Configuration	Experiment Type	Hor. Resolution
CTRL	Control, REMAP Option 2	AMIP (30 yrs.)	C180
CSRAD	Chou-Suarez (1994) Shortwave (SW) Radiation	AMIP (30 yrs.)	C180
M2REMAP	MERRA-2 REMAP Option 1 (cubic)	AMIP (30 yrs.)	C180
CSRAD+M2REMAP	Chou-Suarez (1994) SW REMAP Option 1 (cubic)	AMIP (30 yrs.)	C180
LINEAR	MERRA-2 REMAP Option 1 (linear)	EMIP (30 mem.)	C180, C360
QUADRATIC	MERRA-2 REMAP Option 1 (quadratic)	EMIP (30 mem)	C180, C360
CUBIC	MERRA-2 REMAP Option 1 (cubic)	EMIP (30 mem)	C180, C360
CTRL-DAS	Control	DAS (1 yr.)	C180, C360
CUBIC-DAS	REMAP Option 2 MERRA-2 REMAP Option 1 (cubic)	DAS (1 yr.)	C180, C360

erwise seem innocuous. They also provide further evidence of the strong influence of tropical lower stratospheric upwelling strength on stratospheric mean age in GEOS.

Finally, in all experiments using REMAP Option 1 (i.e. M2REMAP, CSRAD+M2REMAP, LINEAR, QUADRATIC, CUBIC) additional modifications to the divergence damping coefficients were used so as to best ensure consistency with what was used in MERRA-2. Specifically, these include changes to the number of layers for vertical sub-grid mixing, the DAS coefficient for barotropic mode damping, the use of 2nd vs. 6th order divergence damping and the strength of the divergence damping coefficients.

Amal, need description of two DAS runs.

2.3 Analysis Approach

2.3.1 Transport Diagnostics

To diagnose the transport circulation we focus primarily on the age-of-air (Hall and Plumb (1994)). This is inferred from an idealized global “clock” or ideal age tracer (Γ) (Thiele and Sarmiento (1990)) that is defined with respect to the first model level as follows: initially, the ideal age tracer is set to zero throughout the troposphere and thereafter held to zero over the entire Earth’s surface, subject to a constant aging of 1 year/year throughout the atmosphere. We present here the statistically stationary (equilibrated) value of $\Gamma(r)$, which is equal to the average time since the air at a location r in the stratosphere last contacted the Earth’s surface. In addition to the mean age, we also show results from an idealized e90 tracer that is uniformly emitted over the entire surface layer and decays exponentially at a rate of 90 days⁻¹ such that concentrations greater than 125 ppb and less than 50 ppb tend to reside in the lower troposphere and stratosphere, respectively (Prather et al. (2011)). As this tracer features strong near-tropopause gradients and takes significantly less time to equilibrate, compared to the mean age, it is useful for evaluating stratosphere-troposphere-exchange and transport within the upper troposphere/lower stratosphere (Abalos et al. (2017, 2020); Orbe et al. (2020)).

Both the mean age and e90 tracers were integrated in all of the AMIP experiments shown in Figure 1 and listed in Table 2 (rows 1-4), which were run using the same idealized passive tracer package described in Orbe et al. (2017). Note that the mean age tracer was not integrated in the EMIP or DAS experiments given its much longer characteristic timescale in the stratosphere (\sim 3-5 years). As such, the EMIP and DAS simulations, which do not exceed one year, are not appropriate for evaluating the time-integrated transport characteristics reflected in the age-of-air.

In addition to carrying the idealized tracers, two of the experiments shown in Figure 1 were also run with full interactive chemistry and correspond to the two CCMI (Phase 1 and Phase 2) integrations (red and green lines, Figure 1). Both simulations employ the same Global Modeling Initiative (GMI) chemical mechanism (Strahan et al. (2013)) and are therefore useful in evaluating the impact of age differences on real trace gas distributions. In particular, as shown in Section 3.1 results from these experiments show significant imprints of the age-of-air changes on nitrous oxide (N_2O) and methane (CH_4).

2.3.2 Circulation Diagnostics

As we show in Section 3, the changes in age-of-air across the different model versions are strongly tethered to changes in the advective component of the circulation, which we quantify using the Transformed Eulerian Mean (TEM) estimate of the Lagrangian transport of mass by the circulation. Thus, in addition to more standard Eulerian metrics of the circulation (e.g., zonal winds and temperatures), we focus on the vertical component of the TEM residual velocity, defined as $\bar{w}^* = \bar{w} + \frac{\partial(\psi \cos\phi)}{a \cos\phi \partial\phi}$, where $\psi = \overline{v'\theta'}/\frac{\partial\bar{\theta}}{\partial p}$ is the eddy stream function, θ refers to potential temperature, a is the Earth’s radius

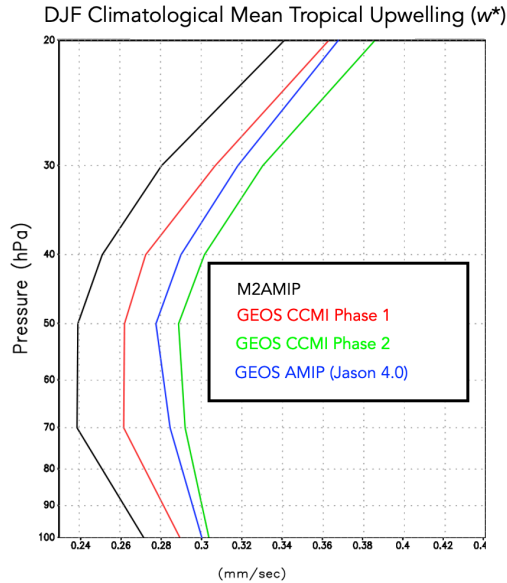


Figure 2. The DJF 1985-1994 climatological mean vertical residual mean velocity, w^* , averaged between the turnaround latitudes for GEOS model configurations corresponding to the CCM1 Phase 1 (red) and Phase 2 (green) submissions and to Jason 4.0 GEOS AMIP (blue). M2AMIP is shown in black.

343 and overbars and primes denote zonal means and deviations therefrom, respectively (Andrews
 344 et al. (1987)). In addition, we interpret the behavior in w^* using the Eliassen-Palm flux
 345 divergence ($\nabla \cdot \mathbf{F}$), whose horizontal ($F(\phi)$) and vertical ($F(p)$) components are respec-
 346 tively defined as $F(\phi) = \text{acos}\phi \left[\frac{\partial u}{\partial p} \psi - \overline{u'v'} \right]$ and $F(p) = \text{acos}\phi \left[\left[f - \frac{\partial u \text{cos}\phi}{\text{acos}\phi \partial \phi} \right] \psi - \overline{u'\omega'} \right]$.

347 2.4 Observations and Reanalyses

348 While our focus is on interpreting and understanding the different model config-
 349 urations, we incorporate observations to provide context when possible, although we do
 350 not present an exhaustive evaluation of the model's transport characteristics (for that
 351 see earlier studies including Orbe et al. (2017, 2018)). However, as the tracers are not
 352 directly integrated in MERRA-2 (with the exception of ozone), we compare against in-
 353 dependent observational estimates. For the mean age we first compare simulated merid-
 354 ional age profiles at 50 hPa with values derived from in situ aircraft measurements of car-
 355 bon dioxide (CO_2), averaged in 2.5 degree latitude bins over the altitude range 19.5 to
 356 21.5 km (Boering et al. (1996), see also Figure 5 in Hall et al. (1999)).

357 We also briefly evaluate impacts of transport biases on the simulated trace gas dis-
 358 tributions for the CCM1 Phase 1 and 2 experiments. The simulated fields of methane
 359 (CH_4) are compared with the climatologies derived for 1991–2002 from the Halogen Oc-
 360 culation Experiment (HALOE) on board the Upper Atmosphere Research Satellite (UARS)
 361 (Groß and Russell III (2005)). Comparisons of simulated nitrous oxide (N_2O) are made
 362 against 2005–2015 climatologies derived from the Microwave Limb Sounder (MLS) on
 363 the Earth Observing System (EOS) Aura satellite. We use the 190-GHz retrieval from
 364 Version 4.2 because the 640-GHz data set ends in summer 2013 due to the failure of the
 365 N_2O primary band.

366 For the circulation diagnostics nearly all comparisons are made relative to MERRA-
 367 2 and comparisons against ERA-5 (not shown) reveal a similar picture. One exception,
 368 however, is the vertical component of the TEM circulation (w^*), which shows some dif-
 369 ferences in vertical structure between MERRA-2 and a 30-member ensemble of (free-running)
 370 AMIP integrations produced using the MERRA-2 model, hereafter referred to as MA2AMIP
 371 (Collow et al., 2017)(Appendix Figure A1, right). This difference in vertical structure
 372 may reflect differences in the vertical levels used to calculate the (highly derived) TEM
 373 circulation, which is notoriously sensitive not only to differences in the formulation of
 374 the equations (Hardiman et al., 2010), but also to the vertical resolution of the input ve-
 375 locities and associated heat and momentum fluxes that are used to calculate the verti-
 376 cal derivatives in the eddy stream function (Gerber & Manzini, 2016). Regardless of the
 377 reason, it is essential that comparisons of the simulated TEM velocities be made using
 378 consistent calculations; therefore, when comparing the TEM circulation in the A(E)MIPS,
 379 in lieu of MERRA-2 we use results from M2AMIP. This ensures as apples-to-apples com-
 380 parison of the TEM in the various GEOS experiments with the MERRA-2 system as pos-
 381 sible (note that for non-derived measures (i.e., winds, temperatures) the raw MERRA-
 382 2 output is used).

383 3 Results

384 3.1 Reduction of Stratospheric Mean Age in GEOS Models 385 Since MERRA-2

386 We begin by interpreting the reduction in mean age exhibited in more recent model
 387 versions in terms of changes in the strength of upwelling in the tropical lower stratosphere.
 388 In particular, the reductions in Γ (Figure 1) are consistent with increases in the strength
 389 of lower stratospheric tropical upwelling, with w^* becoming progressively stronger in more
 390 recent model tags, relative to MERRA-2 (Figure 2). Though perhaps naive, this rela-
 391 tionship between lower stratospheric upwelling and the mean age is consistent with the
 392 long-term behavior of Γ inferred from both historical and projected future climate sim-
 393 ulations (Butchart et al. (2010); Abalos et al. (2021)). A strong relationship between the
 394 strength of lower stratospheric ascent and the mean age was also shown to hold in the
 395 CCMVal models (see Fig. 5.20 in J. Neu et al. (2010)). Nevertheless, it is important to
 396 note that a clear relationship between w^* and Γ is not a priori expected, as the age-of-
 397 air is also known to be very sensitive to mixing, which may be important in interpret-
 398 ing differences among the CCM1 Phase 1 models (Dietmüller et al. (2018)).

399 The differences in w^* highlighted in Figure 2 are associated with enhanced Eliassen-
 400 Palm flux convergence over NH midlatitudes (Figure 3). Increased wave convergence is
 401 evident not only within the subtropical lower stratosphere ($< 30^\circ\text{N}$, 50-100 hPa) but also
 402 over higher latitudes and altitudes ($\sim 40^\circ\text{-}70^\circ\text{N}$, 20-50 hPa). The fact that differences
 403 in extratropical wave convergence imprint on tropical upwelling is consistent with our
 404 understanding of the so-called “downward control” principle (Haynes et al. (1991)).

405 In particular, the strength of the residual mean streamfunction (Ψ^*) is, via down-
 406 ward control, directly related to the vertically integrated eddy-induced total zonal force
 407 above that level and has contributions both from the (resolved wave) Eliassen-Palm flux
 408 divergence (Figure 3) as well as parameterized waves (not shown). The tropical upward
 409 mass flux – defined as $\Psi_{\max}^* - \Psi_{\min}^*$ evaluated at the turnaround latitudes (e.g. Rosenlof
 410 (1995)) – is therefore directly dependent on the wave forcing aloft.

411 One subtlety to note is that the wave convergence changes shown in Figure 3 oc-
 412 cur at high latitudes and are directly associated with downwelling over the polar region.
 413 It is then via mass balance that anomalously strong downwelling associated with enhanced
 414 flux convergences must be accompanied by enhanced upwelling in the tropics. This in-
 415 direct impact of higher latitude wave drag comprise an “extratropical pumping” mech-

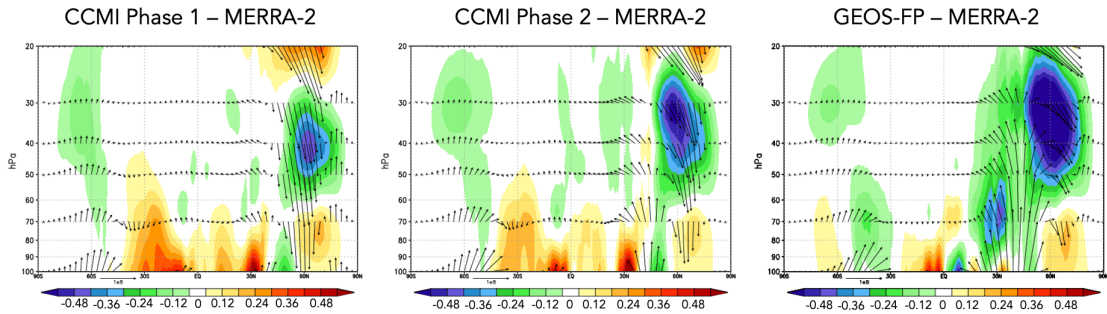
DJF Climatological Mean Eliassen-Palm Flux Divergence ($\nabla \cdot \mathbf{F}$)

Figure 3. Colors show anomalies in the DJF climatological mean Eliassen-Palm (EP) flux divergence between the CCMI Phase 1 (left), CCMI Phase 2 (middle) and Jason 4.0 GEOS AMIP (right) model versions, relative to MERRA-2. Arrows denote anomalies in the vertical and meridional EP flux vectors (relative to MERRA-2).

416 anism Holton et al. (1995), illustrated more clearly in Section 3.2 in the context of the
 417 LINEAR, QUADRATIC and CUBIC experiments.

418 While the reduction in Γ (Figure 1) of $\sim 30\%$ at 50 hPa is significant, it is neither
 419 clear if this change is representative of other altitudes within the stratosphere nor how
 420 this age bias imprints on real chemical species. To this end, we begin by comparing the
 421 full latitude-pressure distribution of changes in Γ and another passive tracer (e90) (Fig-
 422 ure 4) between the CCMI Phase 1 and Phase 2 model configurations (red and green lines,
 423 Figure 1). In particular, we find that the changes in both passive tracers – large reductions
 424 in Γ within both hemispheres (Fig. 4, top right) and increased values of e90 within
 425 the lower stratosphere (Fig. 4, bottom right) – are reflective of an overall increase in the
 426 strength of the transport circulation. This is highlighted in the CCMI Phase 2 – 1 model
 427 differences for the passive tracer distributions (Fig. 4, right panels) which are shown in
 428 the absence of robust observational constraints of Γ at higher altitudes (or any obser-
 429 vational constraints for e90, for that matter). The reduced/increased stratospheric bur-
 430 dens of the age and e90 tracers are consistent with stronger upwelling in the CCMI Phase
 431 2 model configuration (Figure 2).

432 While the observational constraints on Γ presented in Figure 1 and the departure
 433 of w^* away from MERRA-2 suggest that transport properties of the newer model con-
 434 figurations are moving in the wrong direction, it is relevant to ask whether or not the
 435 trace gas satellite measurements also support this conclusion. Indeed, comparisons with
 436 observations show larger biases in N_2O (Fig. 5, top panels) and CH_4 (Fig. 5, bottom pan-
 437 els), increasing from 10% to 30% in the CCMI Phase 2 model configuration, depending
 438 on the species. The patterns of these biases are generally consistent with the biases in
 439 the mean age (Fig. 4), suggesting a strong link between the tracers. Recall that the same
 440 chemistry mechanism is used in both CCMI Phase 1 and 2 simulations.

441 The fact that the mean age changes have a significant imprint on the simulated trace
 442 gases is consequential for the GEOS-R21C system. However, the configurations shown
 443 in Fig. 1-5 differ in many respects (physics, resolution, radiation, FV remapping algo-
 444 rithm) and it is difficult to meaningfully interpret what is driving the changes in w^* (and
 445 the tracers). We therefore move next to the targeted model experiments (Table 2) in or-

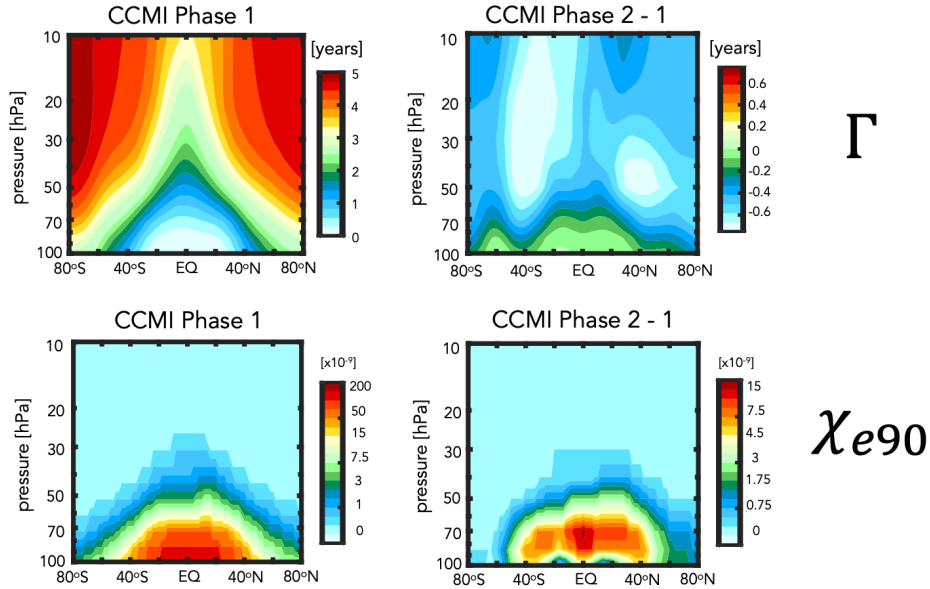


Figure 4. The climatological mean (2000-2010) distribution of the mean age-of-air (Γ) (left, top) and e90 idealized tracers (left, bottom) for the CCMI Phase 1 model configuration. Climatological differences between the CCMI Phase 2 and Phase 1 model configurations are shown in the right panels. Note that a nonlinear colorbar has been used in the e90 subplots.

446 der to interpret the model development steps that resulted in these transport circula-
 447 tion changes.

448 **3.2 Identifying Drivers of Upwelling and Tracer Changes Since** 449 **MERRA-2**

450 **3.2.1 Radiation versus REMAP Algorithm**

451 As discussed in Section 2, among the model changes that were made since MERRA-
 452 2, the changes in radiation and the FV remapping algorithm are most likely to directly
 453 have impacted the stratospheric circulation. We therefore begin by assessing which of
 454 these changes dominates the decreases in Γ shown in Figure 1.

455 Figure 6 shows the distribution of Γ for experiments in which the shortwave radi-
 456 ation and REMAP updates since MERRA-2 have successively been undone. Relative to
 457 the control experiment (CTRL; Table 2, row 1), the reversion back to Chou (1992) in
 458 the shortwave results in an increase in the mean age of ~ 0.5 years throughout the strato-
 459 sphere (CSRAD; Table 2, row 2). Though significant, this change in Γ is smaller than
 460 the change that results from reverting back to REMAP Option 1 (M2REMAP; Table
 461 1; row 3), in which the mean age increases by ~ 1 year. The combined impacts of both
 462 changes (CSRAD+M2REMAP; Table 1 row 4) is roughly linear, with age values of \sim
 463 5.5 years over high latitudes at 50 hPa, consistent with the values simulated by the GEOS-
 464 CTM MERRA-2 integration (black line, Figure 1) and with the CCMI Phase-1 version
 465 of the model (red line, Figure 1).

466 Next we ask if the behavior of Γ exhibited in Figure 6 can be interpreted in terms
 467 of changes in the strength of lower stratospheric tropical upwelling and extratropical wave

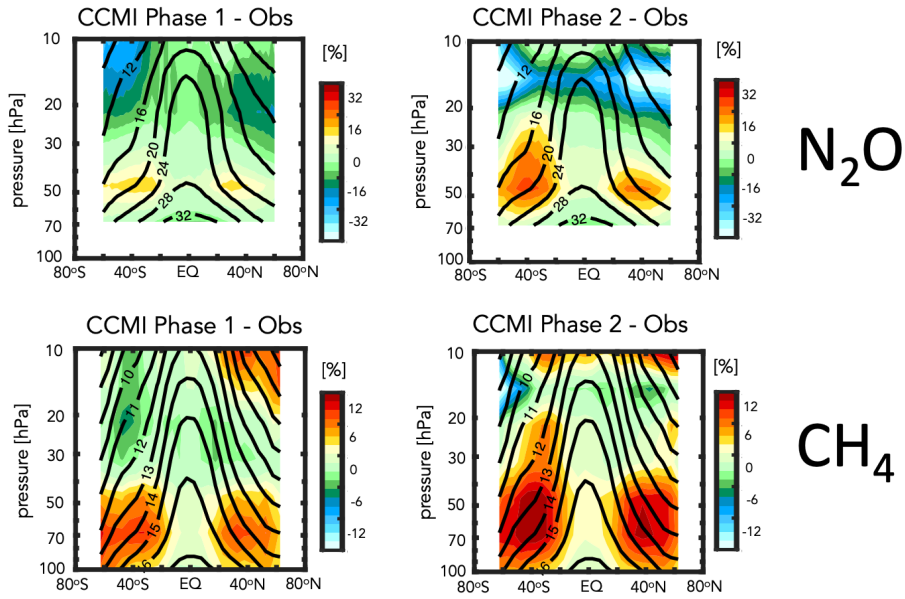


Figure 5. Colors shown anomalies in the simulated distributions of nitrous oxide (N_2O) (top) and methane (CH_4) (bottom), relative to the MLS and HALOE observed values, respectively, for the CCMI Phase 1 (left) and Phase 2 (right) GEOS model configurations. Climatological mean observed values are shown in the black contours.

Annual Climatological Mean Stratospheric Mean Age (Γ)

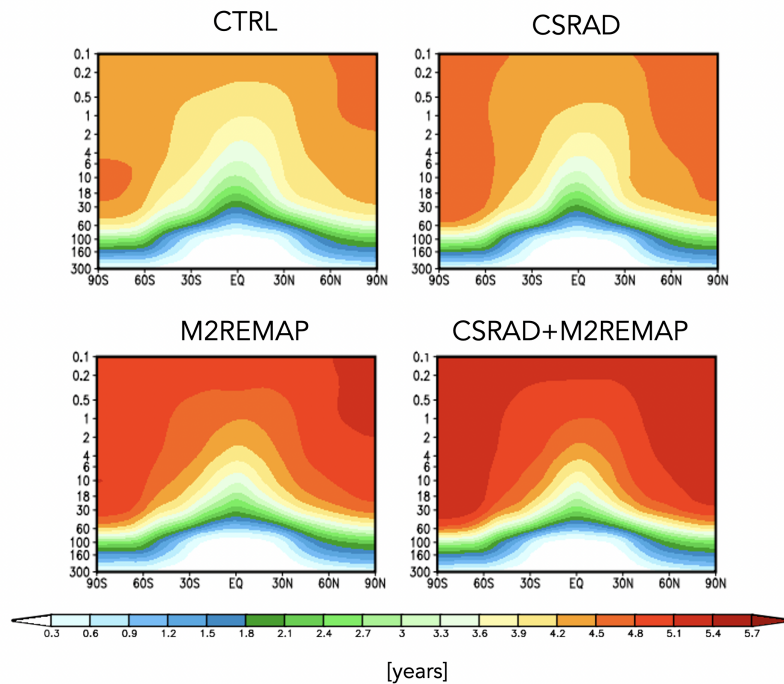


Figure 6. Colors show the simulated 2000-2010 climatological annual mean distributions of the mean age-of-air (Γ) for the CTRL (top left; Table 1, row 1), CSRAD (top right; Table 1, row 2), M2REMAP (bottom left; Table 1, row 3) and combined CSRAD+M2REMAP (bottom right; Table 1, row 4) experiments.

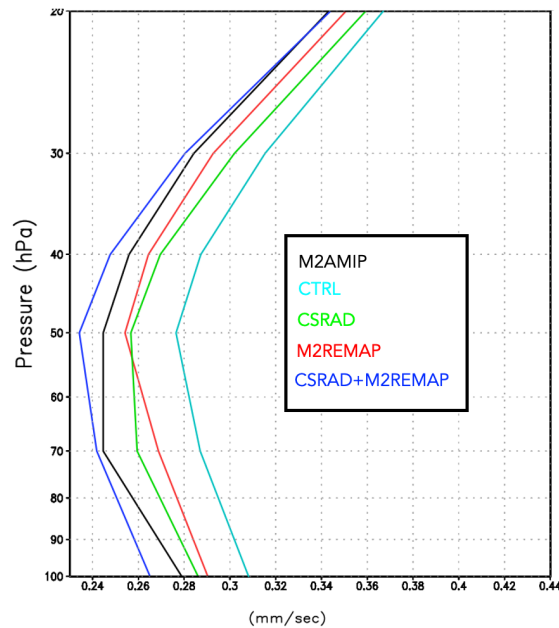
DJF Climatological Mean Tropical Upwelling (w^*)

Figure 7. The DJF climatological mean vertical residual mean velocity, w^* , averaged between the turnaround latitudes for the CTRL (cyan line; Table 2, row 1), CSRAD (green line; Table 2, row 2), M2REMAP (red line; Table 2, row 3) and combined CSRAD+M2REMAP (blue line; Table 2, row 4) experiments. M2AMIP is shown in black.

468 convergence, as our previous analysis of the CCMi experiments suggested. Indeed, Fig-
 469 ure 7 shows that values of upwelling decrease in the CSRAD and M2REMAP experiments,
 470 relative to the CTRL integration. The increase in upwelling resulting from both changes
 471 (CSRAD+M2REMAP) is still larger, consistent with the larger age decreases in that ex-
 472 periment. This change in the behavior of w^* within the tropical stratosphere can be in-
 473 terpreted in terms of changes in the Eliassen Palm flux convergence over NH midlati-
 474 tudes (not shown), which features smaller values in the CSRAD, M2REMAP (and CSRAD+
 475 MSREMAP) experiments. Note that our examination of the changes in w^* are derived
 476 from EMIP integrations, which we showed previously converge (for DJF) to the statis-
 477 tics derived from corresponding AMIP experiments.

478 3.2.2 FV REMAP Algorithm: Sensitivity of Climate Statistics

479 Having shown in the previous section that the largest changes in the mean age were
 480 realized through the reversion back to REMAP Option 1, we now investigate further the
 481 sensitivity of the transport circulation to the choice of remapping interpolation scheme.
 482 In particular, we compare simulations in which total energy is calculated at new mid-
 483 layer pressures using cubic, quadratic and linear interpolation prior to the aposterior in-
 484 tegral conservation (Table 2, rows 5-7). In addition, in this section we seek to understand
 485 how the changes in the Eliassen-Palm flux convergence over NH midlatitudes arise via
 486 analysis of the large-scale wind structure.

487 Figure 8 (left panels) shows a clear sensitivity in tropical upwelling to the choice
 488 of interpolation scheme, with w^* progressively increasing in strength moving from the
 489 CUBIC to QUADRATIC to LINEAR schemes. This sensitivity is robust across horizon-

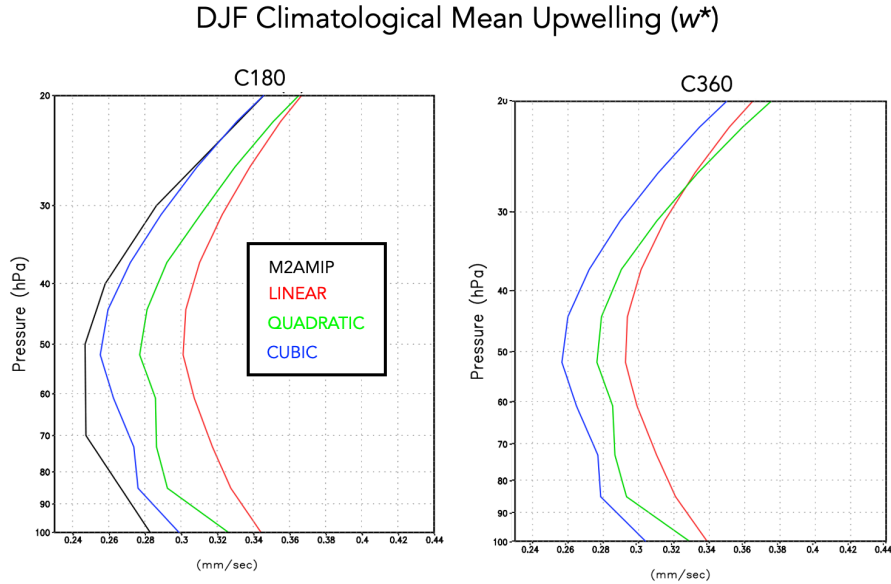


Figure 8. The DJF climatological mean vertical residual mean velocity, w^* , averaged between the turnaround latitudes for the LINEAR (red line; Table 2, row 5), QUADRATIC (green line; Table 2, row 6) and CUBIC (blue line; Table 2, row 7) experiments. M2AMIP is shown in black. Results from C180 and C360 EMIP experiments are shown in the left and right panels, respectively.

490 tal resolutions as the same suite of experiments performed at C360 exhibit the same sensi-
 491 tivity (Fig. 8, right panels). While no current model tag actually employs a linear scheme,
 492 this suite of experiments highlights the strong sensitivity to choice of interpolation scheme
 493 within the remapping algorithm; to the best of our knowledge, this result has not been
 494 reported in the literature. Furthermore, as we show next, this clean set of experiments
 495 allow us to inquire mechanistically into the processes that are driving the changes in wave
 496 convergence over midlatitudes, unencumbered by differences in horizontal resolution, physics,
 497 etc.

498 Consistent with our expectations based on the analysis of the previous experiments,
 499 the drivers of the changes in w^* are related to increased wave convergence moving from
 500 the CUBIC to QUADRATIC to LINEAR schemes (Figure 9). Over extratropical lati-
 501 tudes, the zonal force associated with this enhanced wave convergence is associated with
 502 enhanced downwelling at high latitudes that, through mass balance, is accompanied by
 503 enhanced upwelling in the tropics. This indirect impact of higher latitude wave drag is
 504 evident in Appendix Figure C1, which show stronger upwelling/downwelling in the LIN-
 505 EAR and QUADRATIC experiments over the tropics/polar region.

506 Next we exploit the fact that these experiments only differ with respect to the in-
 507 terpolation scheme in order to inquire further into the drivers of the wave convergence
 508 changes. To this end, Figure 10 compares profiles of the zonal mean zonal wind between
 509 the CUBIC, QUADRATIC and LINEAR experiments, averaged over the region of en-
 510 hanced wave convergence (i.e. 20°N-60°N). The experiments featuring stronger wave con-
 511 vergence (LINEAR and QUADRATIC) are also simulations with stronger zonal winds,
 512 relative to MERRA-2, especially above 70 hPa. This change in winds occurs at both C180
 513 (Fig. 10, left panel) and C360 (Fig. 10, right panel) resolutions.

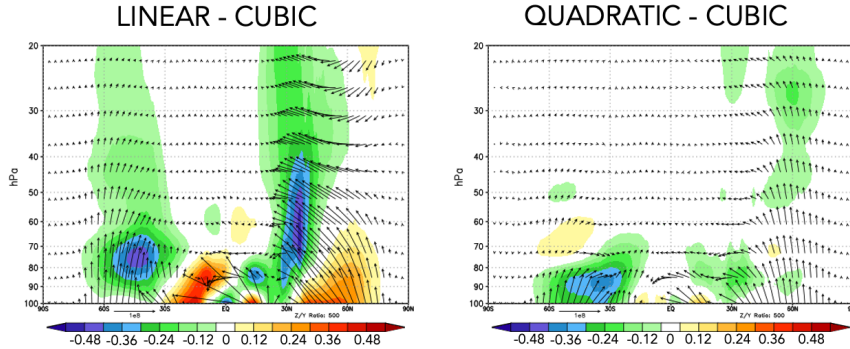
DJF Climatological Mean Eliassen-Palm Flux Divergence ($\nabla \cdot \mathbf{F}$)

Figure 9. Colors shown anomalies in the DJF climatological mean Eliassen-Palm (EP) flux divergence in the LINEAR (left) and QUADRATIC (right) experiments, relative to the CUBIC model experiment. Arrows denote anomalies in the vertical and meridional EP flux vectors.

514 Structurally, the increase in zonal wind strength over northern extratropical mid-
 515 latitudes is reflective of a poleward shift in the zonal winds as the critical latitude, i.e.
 516 where the zonal wind is zero, shifts northward in the QUADRATIC and, especially, LIN-
 517 EAR integrations, relative to the CUBIC experiment (Figure 11). Since stationary waves
 518 only propagate in westerly zonal flow, the latitude where zonal flow is zero acts a bound-
 519 ary for wave propagation (Hardiman et al. (2014)). As a result, this shift in critical lat-
 520 itude results in enhanced wave propagation in that region.

521 Figures 10 and 11 highlight how the changes in zonal winds in the LINEAR and
 522 QUADRATIC experiments reflect a degradation in model skill, relative to MERRA-2,
 523 throughout the entire stratosphere. The changes in upwelling, mean age, chemical trace
 524 gases and zonal winds thus provide a coherent and self-consistent picture suggestive of
 525 a degradation in the representation of the stratospheric circulation since MERRA-2. That
 526 is, an increased bias in the stratospheric northern zonal winds are, via their influence on
 527 wave convergence, compromising changes in the strength of the mean meridional over-
 528 turning circulation and its impact on composition. It is interesting to note that the wind
 529 biases also extend into the troposphere and show degraded skill relative to MERRA-2
 530 in the LINEAR and QUADRATIC experiments (Figure 11). Examination of other fields
 531 (i.e. tropopause biases, Appendix Figure D1) present somewhat more of a nuanced story
 532 that depends more sensitively on latitude and season considered. The improvements in
 533 the zonal winds, however, are most relevant for setting the upwelling characteristics within
 534 the tropical lower stratosphere via their influence on wave propagation into that region.

535 Finally, to better understand why these impacts on the winds have such a conse-
 536 quence for the wave convergence properties within the stratosphere, next we examine the
 537 zonal structure of these biases in the middle stratosphere (Figure 12). This reveals that
 538 the enhanced winds in the LINEAR (and, to a lesser extent, QUADRATIC) integrations
 539 are concentrated over the North Pacific at both C180 (Fig. 12, left) and C360 (Fig. 12,
 540 right) resolutions (a similar picture emerges within the troposphere, not shown). As this
 541 region is the primary region dominating the stationary component of the upward flux
 542 of vertical wave activity (Plumb (1985), see their Figure 4) it is perhaps not surprising
 543 that this region is having a profound impact on the mean overturning circulation. Again,
 544 as with the zonal mean wind changes, the increases in wind strength over the North Pa-

DJF Climatological Mean Zonal Wind (20°N-60°N)

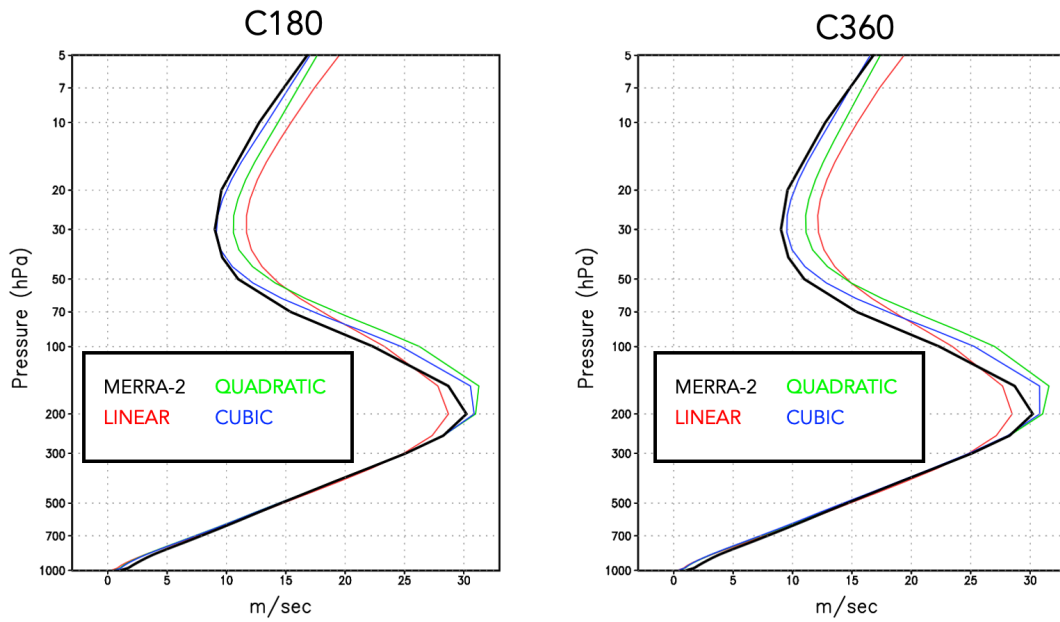


Figure 10. Vertical profiles of the DJF climatological mean zonal mean zonal winds in the LINEAR (red), QUADRATIC (green) and CUBIC (blue) experiments, averaged between 20°N and 60°N. MERRA-2 is shown in the black line. Results for both C180 (left) and C360 (right) experiments are shown.

DJF Climatological Zonal Mean Zonal Wind Anomalies Relative to MERRA-2

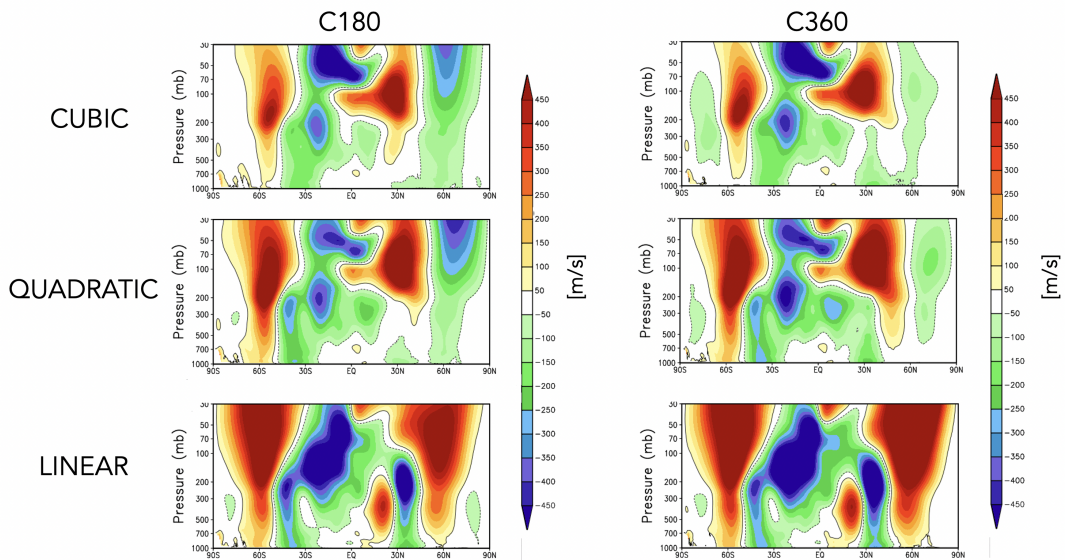


Figure 11. Colors shown anomalies in the DJF climatological mean zonal mean zonal winds in the CUBIC (top), QUADRATIC (middle) and LINEAR (bottom) experiments, relative to MERRA-2. Results for both C180 (left) and C360 (right) experiments are shown.

DJF Climatological 30 hPa Zonal Wind Anomalies Relative to MERRA-2

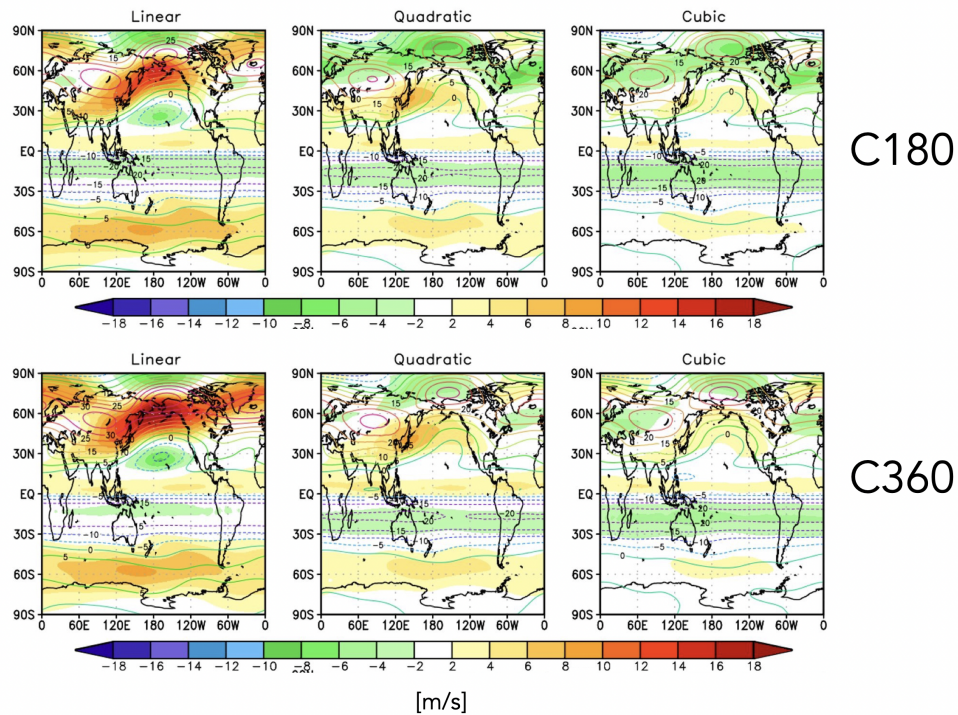


Figure 12. Colors shown anomalies in the DJF climatological mean zonal winds at 30 hPa in the CUBIC (right), QUADRATIC (middle) and LINEAR (left) experiments, relative to MERRA-2. Results for both C180 (top) and C360 (bottom) experiments are shown.

545 cific represent degraded model skill relative to MERRA-2. Note that comparisons with
 546 ERA-5 reveal a similar bias (not shown).

547 *3.2.3 FV REMAP Algorithm: Sensitivity of DAS Analysis State*

548 Up to this point our focus has been on evaluating the various model configurations
 549 via use of 30-year long AMIPs, which are required for deriving the integrated transport
 550 statistics (i.e. age-of-air) that reflect the long timescales relevant to setting the strato-
 551 spheric transport circulation. However, this not only poses practical challenges for model
 552 development purposes (which may be ameliorated, for some variables, through use of EMIPs),
 553 but it is also not obvious how the time-integrated model biases inferred from AMIPs man-
 554 ifest in a data assimilation (DAS) context. To this end, here we briefly comment on im-
 555 plications for the DAS analysis state.

556 In particular, we compare two DAS experiments one mimicking MERRA2 (d46aremp2)
 557 and one mimicking the control configuration (d46actrl) (Table 2, rows 8-9). As in the
 558 previous section, we also consider the robustness of results to changes in horizontal res-
 559 olution.

560 Need to write when receive Amal's new figure (current Figure 13 is only a place-
 561 holder).

PLACEHOLDER

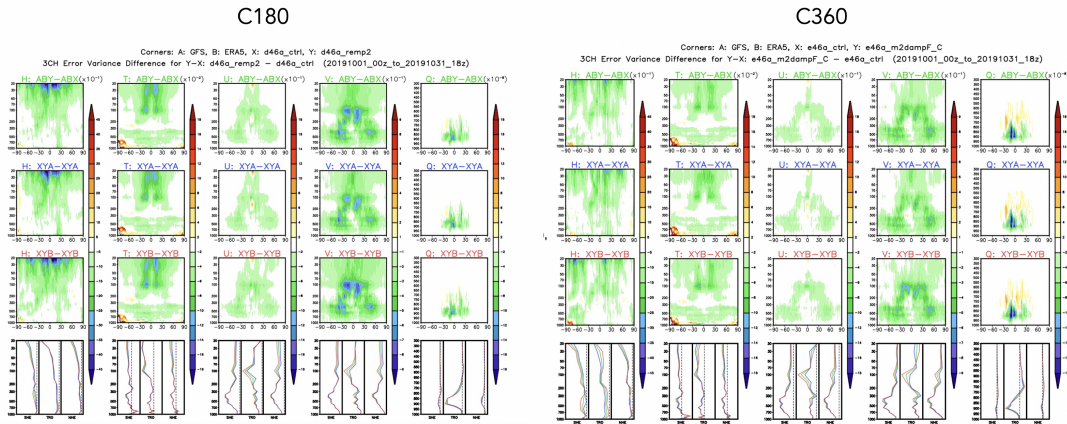


Figure 13. Need to fill in when figure has been decided.

562 4 Conclusions

563 Here we have performed an analysis aimed at understanding differences in the rep-
 564 resentation of the stratospheric circulation in recent candidate systems for GEOS-R21C,
 565 relative to older versions of GEOS similar to the model used to produce MERRA-2. Us-
 566 ing targeted experiments oriented at disentangling various model development updates,
 567 we have identified a key role played by changes in the remapping algorithm within the
 568 model's finite-volume dynamical core. Our key results are as follows:

569 #1. The stratospheric mean age-of-air in GEOS is sensitive to the degree of the
 570 interpolation scheme that is used to calculate layer-mean values of total energy, U, V and
 571 tracers. Different treatment of the vertical remapping algorithm (REMAP Option 1 vs.
 572 2) result in mid-stratospheric (50 hPa) age-of-air differences of ~ 1 year over high lat-
 573 itudes, or about 30% climatological mean values.

574 #2. The age-of-air sensitivities reflect, to first order, changes in the strength of trop-
 575 ical upwelling associated with the Brewer-Dobson circulation which are in turn are driven
 576 by changes in EP flux convergence over northern midlatitudes. Changes in wave conver-
 577 gence reflect shifts in (critical lines of) wave propagation that originate in the troposphere
 578 over the Pacific Ocean, a region of strong upward wave activity.

579 #3. The degradation of age-of-air, upwelling and zonal wind climate statistics man-
 580 ifest in AMIPs, also translate to degradations in the DAS analysis states of a broad range
 581 of variables. These results are are not sensitive to horizontal resolution.

582 Although our focus here has been on the stratospheric transport circulation, mo-
 583 tivating our use of tracer-independent metrics like the age-of-air, our results have clear
 584 implications for constituent transport in the next reanalysis that is currently under de-
 585 velopment (GEOS-R21C). In particular, we showed that the increased age-of-air biases
 586 correspond to increased biases in the representations of CH_4 and N_2O moving from the
 587 CCM1 Phase 1 to Phase 2 model configuration. This comports with well-known corre-
 588 lations between the mean age and stratospheric trace gases, reinforcing the fact that model
 589 transport inaccuracies continue to significantly affect simulations of important long-lived
 590 chemical species in the stratosphere (Hall et al. (1999)).

591 Our results highlight the key role played by model numerics in transport (e.g., Rood
592 (1987)). The sensitivities in the age-of-air documented herein are also consistent in spirit
593 with the findings in Gupta et al. (2020) who showed significant age differences occurring
594 between spectral versus finite-volume numerics. Our results, however, suggest that there
595 remain large sensitivities even within a given (FV) dynamical core. Furthermore, we also
596 show that that statistics derived from long AMIPS also manifest within a data assim-
597 ilation context, which raises important questions as to the degree to which model biases
598 can be ameliorated through assimilation of observations.

599 Looking forward, our findings support and build on the recommendation proposed
600 in Gupta et al. (2020) for the construction of dynamical core benchmark tests aimed at
601 determining how underlying AGCM numerics impact climatological transport proper-
602 ties. In particular, in addition to the age-of-air, the authors propose a range of strato-
603 spheric circulation diagnostics that should be evaluated including the zonal mean zonal
604 winds, eddy temperature variance and zonal spectra of eddy kinetic energy. Our anal-
605 ysis reveals an important role to be played by the climatological zonal mean wind struc-
606 ture as it impacts wave convergence over midlatitudes; we therefore also recommend ex-
607 plicit consideration of the Eliassen Palm flux convergence and tropical upwelling (w^*)
608 fields as they may be crucial for interpreting age-of-air changes.

609 One somewhat incidental – but practical - result from our analysis is that the statis-
610 tics of $\nabla \cdot \mathbf{F}$ and w^* are well approximated by ensembles of so-called EMIP integrations.
611 As these are substantially easier to run than AMIPs these could provide a “first pass”
612 when evaluating new proposed model development changes, without the immediate need
613 to integrate AMIP-style experiments. We emphasize, however, that this statement should
614 only apply to a first stage in model development as the age-of-air will reflect the time
615 integrated impacts of both advection and mixing.

616 Finally, we conclude by noting that, while we have focused on sensitivities within
617 the FV remapping algorithm, our results have highlighted important sensitivities to changes
618 in radiation and, to a lesser extent, changes in parameterized convection. Though not
619 the dominant drivers of the age-of-air changes identified here, the former could poten-
620 tially influence the age both directly through changes in thermal structure and indirectly
621 by modifying wave propagation and/or generation in the troposphere. Future work will
622 focus on examining these impacts.

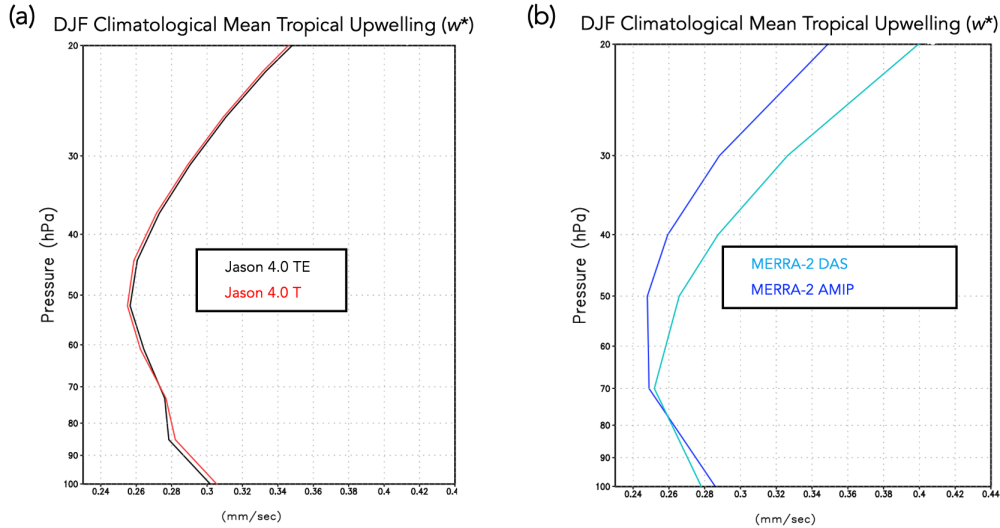


Figure A1. The DJF climatological mean vertical residual mean velocity, w^* , averaged between the turnaround latitudes compared between two Jason 4.0 experiments remapping to temperature (T) (red) versus total energy (TE) (black) (a) and between MERRA-2 DAS (cyan) and the M2AMIP ensemble (blue) (b).

623

Appendix A Sensitivities in Calculation of TEM Upwelling

624

625

626

627

628

629

630

631

632

633

634

635

There are various aspects of the calculation of the TEM circulation that warrant further comment. First, whereas the modeling experiments listed in Table 2 (rows 5-7) focus on the sensitivity of Step 5 in REMAP Option 1 to the choice of interpolation scheme, another difference between REMAP Options 1 and 2 is the use of TE versus T, respectively. To test the impact of this difference, we ran a new experiment (CUBIC-T) which is identical to the CUBIC experiment (Table 2, row 7), except that T is remapped from input layer mean pressure locations to standard output layer mean locations directly using cubic interpolation (i.e., no computation of TE or a-posteriori energy conservation applied). Appendix Figure A1 (a) shows that this has little impact on the strength of tropical upwelling, suggesting that the w^* differences between REMAP Options 1 and 2 are dominated by sensitivities to the choice of interpolation scheme, not the use of TE versus T.

636

637

638

639

640

641

642

643

Second, the vertical component of the TEM circulation (w^*) shows some differences in vertical structure between MERRA-2 and the 30-member M2AMIP ensemble (Appendix Figure A1 (b)). This difference in vertical structure may reflect differences in the output vertical levels used to calculate the (highly derived) TEM circulation, which differ between MERRA-2 and all AMIP experiments (**Larry, is this true?**). To this end, all comparisons of simulated TEM velocities in the AMIPs are made relative to M2AMIP, not MERRA-2. **Even if the previous statement is true, still unsatisfying why DAS and AMIP structures are so different...this needs more work.**

644

Appendix B Correspondence between EMIP and AMIP Upwelling

645

646

Appendix Figure B1 shows the close correspondence in DJF climatological mean w^* , averaged between the turnaround latitudes, from AMIP and EMIP experiments us-

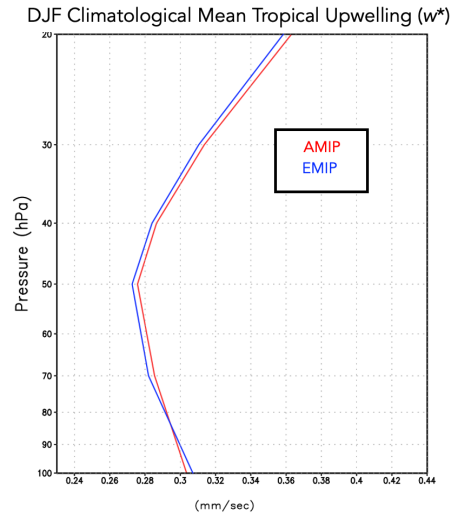


Figure B1. The DJF climatological mean vertical residual mean velocity, w^* , averaged between the turnaround latitudes for the CTRL experiment (Table 2, row 1). Results based on a 30-year-long AMIP experiment (red line) and a 30-member ensemble of three-month-long EMIP experiments (blue line) are shown.

647 ing the same model configuration. This good agreement in upwelling is used to justify
 648 the analysis of the EMIP experiments listed in Table 2 (rows 5-7).

649 **Appendix C Changes in Tropical and High Latitude Upwelling**

650 Appendix Figure C1 compares the behavior in residual mean upwelling among the
 651 LINEAR, QUADRATIC and CUBIC experiments over the latitudes between the (tropi-
 652 cal) turnaround latitudes (left) and poleward of the northern turnaround latitude (right).
 653 The ordering among experiments in both regions reflects how increases in downwelling
 654 at high latitudes are, through mass balance, accompanied by enhanced upwelling in the
 655 tropics.

DJF Climatological Mean Upwelling (w^*)

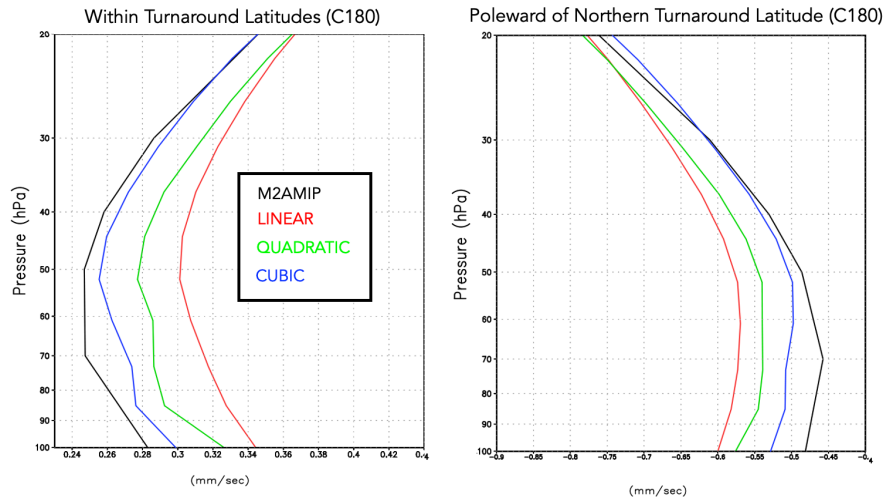


Figure C1. Left: The DJF climatological mean vertical residual mean velocity, w^* , averaged between the turnaround latitudes for the LINEAR (red line; Table 2, row 5), QUADRATIC (green line; Table 2, row 6) and CUBIC (blue line; Table 2, row 7) experiments. M2AMIP is shown in black. Right: As in left panel, except averaged over latitudes poleward of the northern turnaround latitude. Results in both panels are shown for C180 experiments.

656

Appendix D Tropopause Pressure

657

Appendix Figure D1 compares boreal winter tropopause pressure and temperature among the LINEAR, QUADRATIC and CUBIC experiments, relative to MERRA-2.

658

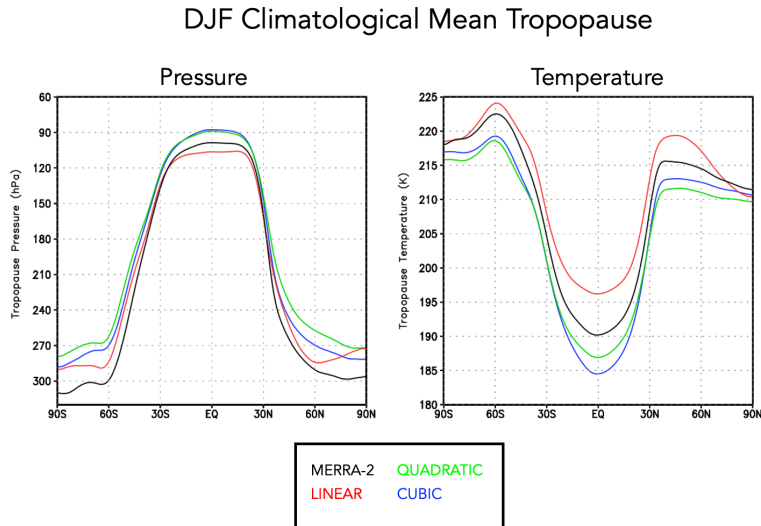


Figure D1. The DJF climatological mean tropopause pressure (left) and temperature (right) in the CUBIC (blue), QUADRATIC (green) and LINEAR (red) experiments. MERRA-2 is shown in black. Results are shown for the C180 experiments.

659 **Acronyms**

- 660 **AMIP** Atmospheric Model Intercomparison Project
 661 **CH₄** methane
 662 **CCMs** chemistry climate models
 663 **CCMI** Chemistry Climate Modeling Initiative
 664 **CCMVal** Chemistry Climate Model Validation
 665 **CO₂** carbon dioxide
 666 **CTRL** control
 667 **CTM** chemistry transport model
 668 **DAS** Data assimilation
 669 **DJF** December-January-February
 670 **EMIP** ??????????
 671 **EOS** Earth Observing System
 672 **EP** Eliassen-Palm
 673 **FV** finite volume
 674 **GEOS** Global Earth Observing System
 675 **GEOS-R21C** GEOS Retrospective analysis for the 21st Century
 676 **GMI** Global Modeling Initiative
 677 **HALOE** Halogen Occultation Experiment
 678 **MERRA-2** Modern-Era Retrospective Analysis for Research and Applications v2
 679 **MLS** Microwave Limb Sounder
 680 **N₂O** nitrous oxide
 681 **NH** northern hemisphere
 682 **PPM** piecewise parabolic
 683 **RRTMG** Rapid Radiative Transfer Model for GCMS
 684 **SW** shortwave
 685 **TE** total energy
 686 **TEM** Transformed Eulerian Mean

687 **UARS** Upper Atmosphere Research Satellite

688 **Open Research Section**

689 TBD

690 **Acknowledgments**

691 C.O. thanks William Putnam and Lawrence Coy for their insight which helped in inter-
 692 preting the results and guiding experimental design. The authors also thank the high-
 693 performance computing resources provided by NASA’s Advanced Supercomputing (NAS)
 694 Division and the NASA Center for Climate Simulation (NCCS) as well as NASA’s Mod-
 695 eling, Analysis and Prediction (MAP) program, which supports the Global Modeling As-
 696 simulation Office and core chemistry-climate and chemistry-modeling activities.

697 **References**

- 698 Abalos, M., Calvo, N., Benito-Barca, S., Garny, H., Hardiman, S. C., Lin, P., . . .
 699 others (2021). The Brewer–Dobson circulation in CMIP6. *Atmospheric*
 700 *Chemistry and Physics*, *21*(17), 13571–13591.
- 701 Abalos, M., Orbe, C., Kinnison, D. E., Plummer, D., Oman, L. D., Jöckel, P., . . .
 702 others (2020). Future trends in stratosphere-to-troposphere transport in CCM1
 703 models. *Atmospheric Chemistry and Physics*, *20*(11), 6883–6901.
- 704 Abalos, M., Randel, W. J., Kinnison, D. E., & Garcia, R. R. (2017). Using the
 705 artificial tracer e90 to examine present and future UTLS tracer transport in
 706 WACCM. *Journal of the Atmospheric Sciences*, *74*(10), 3383–3403.
- 707 Andrews, D., Holton, J., & Leovy, C. (1987). Middle Atmosphere Dynam-
 708 ics. *Academic Press*, *60*, 489. doi: 10.1175/1520-0469(2003)060<0103:
 709 CEOOAL>2.0.CO;2
- 710 Arnold, N. P., Putman, W. M., & Freitas, S. R. (2020). Impact of resolution and
 711 parameterized convection on the diurnal cycle of precipitation in a global
 712 nonhydrostatic model. *Journal of the Meteorological Society of Japan. Ser. II*.
- 713 Boering, K. A., Wofsy, S., Daube, B., Schneider, H., Loewenstein, M., Podolske, J.,
 714 & Conway, T. (1996). Stratospheric mean ages and transport rates from obser-
 715 vations of carbon dioxide and nitrous oxide. *Science*, *274*(5291), 1340–1343.
- 716 Butchart, N., Cionni, I., Eyring, V., Shepherd, T., Waugh, D., Akiyoshi, H., . . .
 717 others (2010). Chemistry–climate model simulations of twenty-first century
 718 stratospheric climate and circulation changes. *Journal of Climate*, *23*(20),
 719 5349–5374.
- 720 Chiodo, G., & Polvani, L. M. (2019). The response of the ozone layer to quadru-
 721 pled CO₂ concentrations: Implications for climate. *Journal of Climate*, *32*(22),
 722 7629–7642.
- 723 Chou, M.-D. (1990). Parameterizations for the absorption of solar radiation by O₂
 724 and CO₂ with application to climate studies. *Journal of Climate*, *3*(2), 209–
 725 217.
- 726 Chou, M.-D. (1992). A solar radiation model for use in climate studies. *Journal of*
 727 *Atmospheric Sciences*, *49*(9), 762–772.
- 728 Chou, M.-D., & Suarez, M. J. (1994). An efficient thermal infrared radiation param-
 729 eterization for use in general circulation models.
- 730 Collow, A. B. M., Mahanama, S. P., Bosilovich, M. G., Koster, R. D., & Schubert,
 731 S. D. (2017). *An evaluation of teleconnections over the united states in an*
 732 *ensemble of AMIP simulations with the MERRA-2 configuration of the GEOS*
 733 *atmospheric model* (Tech. Rep.).
- 734 Davis, N. A., Callaghan, P., Simpson, I. R., & Tilmes, S. (2022). Specified dynamics
 735 scheme impacts on wave-mean flow dynamics, convection, and tracer transport

- 736 in CESM2 (WACCM6). *Atmospheric Chemistry and Physics*, 22(1), 197–214.
- 737 Dietmüller, S., Eichinger, R., Garny, H., Birner, T., Boenisch, H., Pitari, G., ...
- 738 others (2018). Quantifying the effect of mixing on the mean age of air in
- 739 CCMVal-2 and CCM1-1 models. *Atmospheric Chemistry and Physics*, 18(9),
- 740 6699–6720.
- 741 Eichinger, R., Garny, H., Šácha, P., Danker, J., Dietmüller, S., & Oberländer-Hayn,
- 742 S. (2020). Effects of missing gravity waves on stratospheric dynamics: Part 1,
- 743 Climatology. *Climate Dynamics*, 54(5), 3165–3183.
- 744 Eluszkiewicz, J., Hemler, R. S., Mahlman, J. D., Bruhwiler, L., & Takacs, L. L.
- 745 (2000). Sensitivity of age-of-air calculations to the choice of advection scheme.
- 746 *Journal of the Atmospheric Sciences*, 57(19), 3185–3201.
- 747 Eyring, V., Lamarque, J.-F., Hess, P., Arfeuille, F., Bowman, K., Chipperfield,
- 748 M. P., ... others (2013). Overview of IGAC/SPARC Chemistry-Climate
- 749 Model Initiative (CCMI) community simulations in support of upcoming ozone
- 750 and climate assessments. *SPARC Newsletter*, 40(January), 48–66.
- 751 Freitas, S. R., Grell, G. A., Molod, A., Thompson, M. A., Putman, W. M., Santos e
- 752 Silva, C. M., & Souza, E. P. (2018). Assessing the Grell-Freitas convection
- 753 parameterization in the NASA GEOS modeling system. *Journal of Advances*
- 754 *in Modeling Earth Systems*, 10(6), 1266–1289.
- 755 Freitas, S. R., Putman, W. M., Arnold, N. P., Adams, D. K., & Grell, G. A. (2020).
- 756 Cascading toward a kilometer-scale GCM: Impacts of a scale-aware convection
- 757 parameterization in the Goddard Earth Observing System GCM. *Geophysical*
- 758 *Research Letters*, 47(17), e2020GL087682.
- 759 Gelaro, R., McCarty, W., Suárez, M. J., Todling, R., Molod, A., Takacs, L., ...
- 760 others (2017). The modern-era retrospective analysis for research and applica-
- 761 tions, version 2 (MERRA-2). *Journal of Climate*, 30(14), 5419–5454.
- 762 Gerber, E. P., & Manzini, E. (2016). The Dynamics and Variability Model In-
- 763 tercomparison Project (dynvarmip) for CMIP6: assessing the stratosphere–
- 764 troposphere system. *Geoscientific Model Development*, 9(9), 3413–3425.
- 765 Grell, G. A., & Freitas, S. R. (2014). A scale and aerosol aware stochastic convective
- 766 parameterization for weather and air quality modeling. *Atmospheric Chemistry*
- 767 *and Physics*, 14(10), 5233–5250.
- 768 Grooß, J.-U., & Russell III, J. M. (2005). A stratospheric climatology for O₃, H₂O,
- 769 CH₄, NO_x, HCl and HF derived from HALOE measurements. *Atmospheric*
- 770 *Chemistry and Physics*, 5(10), 2797–2807.
- 771 Gupta, A., Gerber, E. P., & Lauritzen, P. H. (2020). Numerical impacts on tracer
- 772 transport: A proposed intercomparison test of Atmospheric General Circula-
- 773 tion Models. *Quarterly Journal of the Royal Meteorological Society*, 146(733),
- 774 3937–3964.
- 775 Hall, T. M., & Plumb, R. A. (1994). Age as a diagnostic of stratospheric transport.
- 776 *Journal of Geophysical Research: Atmospheres*, 99(D1), 1059–1070.
- 777 Hall, T. M., Waugh, D. W., Boering, K. A., & Plumb, R. A. (1999). Evaluation
- 778 of transport in stratospheric models. *Journal of Geophysical Research: Atmo-*
- 779 *spheres*, 104(D15), 18815–18839.
- 780 Hardiman, S. C., Andrews, D. G., White, A. A., Butchart, N., & Edmond, I. (2010).
- 781 Using different formulations of the transformed Eulerian mean equations and
- 782 Eliassen–Palm diagnostics in general circulation models. *Journal of the Atmo-*
- 783 *spheric Sciences*, 67(6), 1983–1995.
- 784 Hardiman, S. C., Butchart, N., & Calvo, N. (2014). The morphology of the Brewer–
- 785 Dobson circulation and its response to climate change in CMIP5 simulations.
- 786 *Quarterly Journal of the Royal Meteorological Society*, 140(683), 1958–1965.
- 787 Haynes, P., McIntyre, M., Shepherd, T., Marks, C., & Shine, K. P. (1991). On the
- 788 “downward control” of extratropical diabatic circulations by eddy-induced
- 789 mean zonal forces. *Journal of the Atmospheric Sciences*, 48(4), 651–678.
- 790 Hegglin, M. I., Brunner, D., Peter, T., Hoor, P., Fischer, H., Staehelin, J., ... Weers,

- 791 U. (2006). Measurements of NO, NO_y, N₂O, and O₃ during SPURT: implica-
 792 tions for transport and chemistry in the lowermost stratosphere. *Atmospheric*
 793 *Chemistry and Physics*, 6(5), 1331–1350.
- 794 Holton, J. R., Haynes, P. H., McIntyre, M. E., Douglass, A. R., Rood, R. B., & Pfis-
 795 ter, L. (1995). Stratosphere-troposphere exchange. *Reviews of Geophysics*,
 796 33(4), 403–439.
- 797 Holzer, M., & Hall, T. M. (2000). Transit-time and tracer-age distributions in geo-
 798 physical flows. *Journal of the atmospheric sciences*, 57(21), 3539–3558.
- 799 Iacono, M. J., Delamere, J. S., Mlawer, E. J., Shephard, M. W., Clough, S. A., &
 800 Collins, W. D. (2008). Radiative forcing by long-lived greenhouse gases: Cal-
 801 culations with the AER radiative transfer models. *Journal of Geophysical*
 802 *Research: Atmospheres*, 113(D13).
- 803 Ivy, D. J., Solomon, S., Calvo, N., & Thompson, D. W. (2017). Observed connec-
 804 tions of arctic stratospheric ozone extremes to Northern Hemisphere surface
 805 climate. *Environmental Research Letters*, 12(2), 024004.
- 806 Kouatchou, J., Molod, A., Nielsen, J., Auer, B., Putman, W., & Clune, T. (2015).
 807 *GEOS-5 chemistry transport model user’s guide* (Tech. Rep.).
- 808 Legras, B., Pissot, I., Berthet, G., & Lefèvre, F. (2004). Variability of the lagrangian
 809 turbulent diffusivity in the lower stratosphere. *Atmospheric Chemistry and*
 810 *Physics Discussions*, 4(6), 8285–8325.
- 811 Lin, S.-J. (2004). A “vertically lagrangian” finite-volume dynamical core for global
 812 models. *Monthly Weather Review*, 132(10), 2293–2307.
- 813 Molod, A., Takacs, L., Suarez, M., & Bacmeister, J. (2015). Development of the
 814 GEOS-5 atmospheric general circulation model: Evolution from MERRA to
 815 MERRA2. *Geoscientific Model Development*, 8(5), 1339–1356.
- 816 Monge-Sanz, B., Chipperfield, M., Simmons, A., & Uppala, S. (2007). Mean age of
 817 air and transport in a CTM: Comparison of different ECMWF analyses. *Geo-*
 818 *physical Research Letters*, 34(4).
- 819 Monge-Sanz, B. M., Bozzo, A., Byrne, N., Chipperfield, M. P., Diamantakis, M.,
 820 Flemming, J., ... others (2022). A stratospheric prognostic ozone for seam-
 821 less Earth system models: performance, impacts and future. *Atmospheric*
 822 *Chemistry and Physics*, 22(7), 4277–4302.
- 823 Morgenstern, O., & Carver, G. D. (2001). Comparison of cross-tropopause transport
 824 and ozone in the upper troposphere and lower stratosphere region. *Journal of*
 825 *Geophysical Research: Atmospheres*, 106(D10), 10205–10221.
- 826 Neu, J., Strahan, S., Braesicke, P., Douglass, A., Huck, P., Oman, L., ... Tegtmeier,
 827 S. (2010). SPARC CCMVal (2010), SPARC Report on the Evaluation of
 828 Chemistry-Climate Models: Chapter 5: Transport. SPARC.
- 829 Neu, J. L., & Plumb, R. A. (1999). Age of air in a “leaky pipe” model of strato-
 830 spheric transport. *Journal of Geophysical Research: Atmospheres*, 104(D16),
 831 19243–19255.
- 832 Oehrlein, J., Chiodo, G., & Polvani, L. M. (2020). The effect of interactive ozone
 833 chemistry on weak and strong stratospheric polar vortex events. *Atmospheric*
 834 *Chemistry and Physics*, 20(17), 10531–10544.
- 835 Orbe, C., Oman, L. D., Strahan, S. E., Waugh, D. W., Pawson, S., Takacs, L. L., &
 836 Molod, A. M. (2017). Large-scale atmospheric transport in GEOS replay simu-
 837 lations. *Journal of Advances in Modeling Earth Systems*, 9(7), 2545–2560.
- 838 Orbe, C., Rind, D., Jonas, J., Nazarenko, L., Faluvegi, G., Murray, L. T., ... oth-
 839 ers (2020). GISS Model E2.2: A climate model optimized for the middle
 840 atmosphere—2. Validation of large-scale transport and evaluation of cli-
 841 mate response. *Journal of Geophysical Research: Atmospheres*, 125(24),
 842 e2020JD033151.
- 843 Orbe, C., Yang, H., Waugh, D. W., Zeng, G., Morgenstern, O., Kinnison, D. E., ...
 844 others (2018). Large-scale tropospheric transport in the Chemistry–Climate
 845 Model Initiative (CCMI) simulations. *Atmospheric Chemistry and Physics*,

- 846 18(10), 7217–7235.
- 847 Pan, L. L., Wei, J., Kinnison, D., Garcia, R., Wuebbles, D., & Brasseur, G. P.
848 (2007). A set of diagnostics for evaluating chemistry-climate models in the ex-
849 tratropical tropopause region. *Journal of Geophysical Research: Atmospheres*,
850 112(D9).
- 851 Pawson, S., Stajner, I., Kawa, S. R., Hayashi, H., Tan, W.-W., Nielsen, J. E., ...
852 Livesey, N. J. (2007). Stratospheric transport using 6-h-averaged winds from
853 a data assimilation system. *Journal of Geophysical Research: Atmospheres*,
854 112(D23).
- 855 Plumb, R. A. (1985). On the three-dimensional propagation of stationary waves.
856 *Journal of Atmospheric Sciences*, 42(3), 217–229.
- 857 Plumb, R. A. (1996). A “tropical pipe” model of stratospheric transport. *Journal of*
858 *Geophysical Research: Atmospheres*, 101(D2), 3957–3972.
- 859 Plumb, R. A. (2002). Stratospheric transport. *Journal of the Meteorological Society*
860 *of Japan. Ser. II*, 80(4B), 793–809.
- 861 Polvani, L. M., Waugh, D. W., Correa, G. J., & Son, S.-W. (2011). Stratospheric
862 ozone depletion: The main driver of twentieth-century atmospheric circulation
863 changes in the southern hemisphere. *Journal of Climate*, 24(3), 795–812.
- 864 Prather, M. J., Zhu, X., Tang, Q., Hsu, J., & Neu, J. L. (2011). An atmospheric
865 chemist in search of the tropopause. *Journal of Geophysical Research: Atmo-*
866 *spheres*, 116(D4).
- 867 Rood, R. B. (1987). Numerical advection algorithms and their role in atmospheric
868 transport and chemistry models. *Reviews of geophysics*, 25(1), 71–100.
- 869 Rosenlof, K. H. (1995). Seasonal cycle of the residual mean meridional circulation
870 in the stratosphere. *Journal of Geophysical Research: Atmospheres*, 100(D3),
871 5173–5191.
- 872 Son, S.-W., Tandon, N. F., Polvani, L. M., & Waugh, D. W. (2009). Ozone hole and
873 Southern Hemisphere climate change. *Geophysical Research Letters*, 36(15).
- 874 Strahan, S., Douglass, A., & Newman, P. (2013). The contributions of chemistry
875 and transport to low arctic ozone in March 2011 derived from aura MLS obser-
876 vations. *Journal of Geophysical Research: Atmospheres*, 118(3), 1563–1576.
- 877 Thiele, G., & Sarmiento, J. (1990). Tracer dating and ocean ventilation. *Journal of*
878 *Geophysical Research: Oceans*, 95(C6), 9377–9391.
- 879 Waugh, D., & Hall, T. (2002). Age of stratospheric air: Theory, observations, and
880 models. *Reviews of Geophysics*, 40(4), 1–1.